Quantification of low Damköhler number turbulent premixed flames

F. Hampp[a], S. Shariatmadar[a], R. P. Lindstedt[a,*]

[a]*Department of Mechanical Engineering, Imperial College, London, SW7 2AZ, UK*

Abstract

Combustion under highly strained conditions or at low Damköhler numbers requires external enthalpy sources to ensure stability. Such flames deviate from the conventional bimodal flame structure and chemically active fluid states become statistically relevant. The current work utilises a multi-fluid analysis in order to quantify the impact of such conditions on a turbulent ($Re_t \simeq 350$) lean ($\Phi = 0.50$) premixed DME / air flame with $Da \simeq 0.29$. The flames were aerodynamically stabilised in a back-to-burnt opposed jet configuration with the temperature of the external enthalpy support varied from $1200 \leq \ T_{HCP}$ (K) ≤ 1600. Simultaneous Mie scattering, CH_2O and OH – PLIF and PIV were used to quantify the transition from spatially distributed chemical reactions to reaction zones that appear flamelet-like. The analysis shows that in the current configuration such structures are only present at high T_{HCP}. By contrast, the low temperature chemistry is continuously active with CH_2O increasingly more spatially distributed with reducing support temperature. The current analysis provides novel insights into low Damköhler number combustion and burning mode transitions by means of

*Corresponding author:
Email address: p.lindstedt@imperial.ac.uk (R. P. Lindstedt)

(i) multi-fluid probability statistics, (ii) the structure of formaldehyde and hydroxyl layers and (iii) their cross–correlation as well as (iv) the underlying strain rate statistics on material surfaces.

Keywords:
Strain rate, Low Damköhler number combustion, Premixed DME flames, Multi-fluid statistics, Low temperature combustion

---

Supplementary material is available (1 Figure, 1 Table).

1. Introduction

Increasingly stringent emission regulations (e.g. for NO_x and particulates) can be met by (partially-) premixed combustor operation under fuel lean conditions at reduced Damköhler (Da) numbers [1]. Related burning modes deviate from bimodal flame structures by creating increasingly distributed preheat and reaction zones [2, 3]. The reaction progress can be controlled by an external enthalpy source [4, 5], e.g. via exhaust gas recirculation (EGR) or reactant preheating. Practical examples include flameless oxidation in gas turbine engines [6] and low NO_x furnaces [7]. High temperature EGR blending can yield complex competition between chain branching and quenching due to the presence of diluents [8]. Chemical and turbulent timescales of the same order of magnitude lead to complex turbulence-chemistry interactions and a spatial distribution of reactive scalars [9–12]. The back-to-burnt (BTB) opposed jet configuration sustains reaction beyond the conventional extinction point by the counter-flowing hot combustion products (HCP) stream [13–

15]. The configuration is particularly advantageous for the investigation of strained [16] low Da flames due to the aerodynamic flame stabilisation [17], individual and accurate control of chemical and turbulent timescales [13] and excellent optical access [18, 19]. Coriton et al. [14] evaluated the impact of temperature and rate of strain on reaction progress and local extinction. Local and intermittent flame extinction was observed for bulk strain rates that exceeded the conventional extinction limit. Hampp and Lindstedt [20, 21] used simultaneous Mie scattering, hydroxyl (OH) planar laser induced fluorescence (PLIF) and particle image velocimetry (PIV) in combination with a statistical multi-fluid analysis. Self-sustained flames were found detached from the stagnation plane and anchored in low strain regions with thermally supported burning characterised by high rates of strain and vorticity. The analysis provided statistical data on chemically active fluid states in addition to reactants and products. Thermally altered regions without the onset of OH producing reactions were found to be statistically significant for $Da < 1$. A variation of the burnt gas state temperature from 1600 to 1800 K showed a distinct impact on turbulence-chemistry interactions in the reacting fluid states [22].

Reaction progress in low Da flames in the BTB geometry is governed by turbulent transport of HCP across the stagnation plane [20], leading to preheating, low temperature chemistry and, potentially, auto-ignition. Formaldehyde (CH_2O) layers have been used as indicators of radical pool build up [23], with the spatially distributed low temperature chemistry regime of n-heptane investigated by Won et al. [24] using hot wire anemometry and simultaneous CH_2O and OH – PLIF. The CH_2O and OH cross-correlation

has been used to identify heat release layers from PLIF measurements [25] and it remains a valid marker for non-flamelet like structures in EGR type moderate or intense low-oxygen dilution combustion [2]. Gordon et al. [26] investigated transient auto-ignition using OH as a flame marker, CH_2O as a precursor for auto-ignition and their cross-correlation to identify heat release. Simultaneous high speed CH_2O / OH – PLIF and tomographic PIV were performed by Osborne et al. [27, 28] with substantial broadening of the CH_2O layer observed with increasing turbulence intensity, while the CH_2O $\times$ OH layers remained thin.

The current study investigates low Damköhler number ($Da = 0.29$) combustion with a turbulent Reynolds number of $Re_t \simeq 350$ of lean ($\Phi = 0.50$) premixed DME / air flames in a BTB opposed jet configuration. The HCP temperature was varied from 1200 – 1600 K. The results provide novel insights into low Da combustion and burning mode transitions by means of (i) multi-fluid probability statistics, (ii) the structure of CH_2O and OH layers and (iii) their cross–correlation as well as (iv) the underlying strain rate statistics on material surfaces.

2. Experimental Setup

The cross fractal grid (CFG) opposed jet burner was operated in a BTB configuration. The facility was originally developed by Geyer et al. [18] and modified to provide multi-scale turbulence at elevated levels free of bulk instabilities [15, 19, 29, 30]. The present geometry is identical to our recent studies [20–22, 31] with the exception of the lower nozzle (LN) flame stabilising grid (see Sec. 2.2). A schematic is provided in the supplementary

material. The premixed DME / air mixture was injected through the upper nozzle (UN) and stabilised against hot combustion products emerging the LN. The nozzle separation (H) was set to one diameter (= 30 mm). The UN reactant flow is defined as negative and the LN counter-flow as positive.

2.1. Upper Nozzle Flow Conditions

Premixed DME / air ($\Phi = 0.50$, $T_0 = 320$ K) was injected through the UN at a constant bulk velocity ($U_b = 11.2$ m s^{-1}). The CFG was installed 50 mm upstream of the UN exit to provide well developed multi-scale turbulence at the nozzle exit. The grid exhibits a blockage ratio of 65 % with a maximum to minimum bar width ratio of 4. The $Re_t = L_I \cdot u_{rms} \cdot \nu_r^{-1} \simeq 350$ was determined by means of the integral length scale of turbulence ($L_I = 3.9 \pm 0.2$ mm) and the velocity fluctuations ($u_{rms} = 1.6$ m s^{-1}) at the nozzle exit using hot wire anemometry data (sampling time 13 s at a rate of 20 kHz). Both properties, and thus the turbulent timescale (τ_I), were maintained constant with a Kolmogorov length scale of $L_\eta = (\nu_r^3 \cdot \varepsilon_r^{-1})^{1/4} \simeq 48$ µm. The rate of dissipation in the reactants was estimated to $\varepsilon_r \simeq u_{rms}^3 \cdot L_I^{-1} = 955$ m^2 s^{-3}. The calculated kinematic viscosity in the reactants was $\nu_r = 17.1 \times 10^{-6}$ m^2 s^{-1}. The chemical timescale (τ_c) of the UN reactant flow was also maintained constant. The laminar burning velocity ($S_L = 0.096$ m s^{-1}) and laminar flame thickness ($\delta_f = 0.82$ mm) based on the 5–95% fuel consumption layer (i.e. inner thickness [32]) were calculated in a strained ($a_b = 75$ s^{-1}) laminar opposed jet twin flame using detailed chemistry [33]. The conditions occupy a nominally identical point in a conventional regime diagram with $Da \simeq 0.29$ and Karlovitz number (Ka) of 64, see Eq. (1).

$$Da = \frac{L_I \cdot S_L}{u_{rms} \cdot \delta_f} \ , \quad Ka = \frac{\delta_f}{S_L} \left(\frac{\nu_r}{\varepsilon_r} \right)^{-1/2} \tag{1}$$

The extinction strain of the twin laminar flame (a_q = 190 s^{-1}) was below the bulk ($a_b = 2 \cdot U_b \ / \ H$ = 750 s^{-1}) and mean turbulent strain (a_I = 3200 s^{-1}) [20]. The extinction temperature (T_q) was 1380 K.

2.2. Lower Nozzle Flow Conditions

The stabilising HCP were obtained using lean premixed H_2 / CH_4 / air flames (see Table 1). The temperature at the lower nozzle exit (T_{HCP}) was measured using a 50 μm R-type thermocouple and controlled from 1200 to 1600 K (rms 4 K) by adjusting the equivalence ratio (Φ) and H_2 / CH_4 blending ratio. Temperature control via inert gas dilution at fixed stoichiometry and fuel composition [20, 21] does not facilitate the desired range including low support temperatures. The addition of CH_4 to H_2 / air flames broadens the regime of stable flame anchoring on the perforated plate (PP) by eliminating instabilities of the lower nozzle flame. The PP had a 50% blockage ratio with 1.0 mm diameter holes and was located 100 mm upstream of the lower nozzle exit. The HCP are in close-to thermochemical equilibrium at the nozzle exit and the products consist primarily (> 99.8 %) of N_2, O_2, H_2O and CO_2. This provides a well defined burnt gas state to the stagnation plane that is used as reference in Sec. 3. Flames could not be stabilised on the perforated plate below 1200 K and this defines the lower T_{HCP} limit. The upper limit of 1600 K was above the weakly strained (75 s^{-1}) adiabatic flame temperature (T_{ad} = 1536 K) of the upper nozzle reactants. Differences in the HCP density were compensated by modest adjustments of the HCP

Table 1: Lower nozzle conditions with the reactant mole fractions (X) (the missing percentile accounts for air), heat loss (HL) to the burner, equilibrium OH concentration at the nozzle exit ($[\mathrm{OH}]_T^{\ddagger}$) and HCP bulk velocity at the nozzle exit (U_{HCP}) and $T_0 = 310$ K.

$T_{HCP} \times 10^3$	[K]	1.20	1.30	1.40	1.50	1.60
Φ	–	0.30	0.38	0.43	0.51	0.62
$X(\mathrm{H_2}) \times 10^{-2}$	–	8.8	9.7	7.6	6.9	6.7
$X(\mathrm{CH_4}) \times 10^{-2}$	–	0.61	1.1	2.2	3.1	4.1
HL	[%]	7.2	8.7	9.2	9.3	8.9
$[\mathrm{OH}]_T^{\ddagger} \times 10^{-3}$	[mol m^{-3}]	7.38	8.40	8.89	9.72	10.8
U_{HCP}	[m s^{-1}]	22.7	23.4	24.1	24.6	25.1

bulk velocity (see Table 1) in order to position the stagnation plane in the proximity of the burner centre, i.e. jet momentum matching.

2.3. Measurement Setup

Simultaneous Mie scattering, PIV, CH_2O and OH – PLIF measurements were performed using the 2^{nd} harmonic of a Litron Nano LG 175-10 Nd:YAG (Mie scattering and PIV) and a frequency tripled Spectra Physics Quanta-Ray Lab-150 Nd:YAG (CH_2O – PLIF) laser. The residual 2^{nd} harmonic of the latter light source was used to pump a Sirah Cobra Stretch dye laser to probe OH via the $Q_1(8)$ line. The three spatially overlapped light sheets (i.e. Mie scattering and PIV at 532 nm, light sheet height $H_{LS} = 27$ mm, pulse power $P_l \simeq 30$ mJ; CH_2O – PLIF at 355 nm, $H_{LS} = 18$ mm, $P_l \simeq 150$ mJ; OH – PLIF at 283.55 nm, $H_{LS} = 18$ mm, $P_l \simeq 14$ mJ) were located symmetrically around the theoretical stagnation plane. The light sheet thickness was estimated to $\sim$100 µm in the centre of the interrogation region using burn marks. The first pulse of the Mie scattering was recorded 200 ns prior to the LIF signals in order to eliminate elastic scattering in the LIF detection systems. Dichroic filters were used to spatially and spectrally segregate the

signals. The PIV camera (LaVision LX 8M) was equipped with a 180 mm f/2.8 Sigma lens and a narrow width bandpass filter centred at 532 nm. Two LaVision intensifier relay optic units and imager intense cameras were used to the record the CH_2O and OH – PLIF signals. The former was equipped with a 85 mm (f/1.2) lens and a 400 nm long-pass filter due to the absence of polycyclic aromatic hydrocarbons (PAH) interference [34]. The OH – PLIF was recorded using a 105 mm UV lens (f/2.8) and a filter combination that featured an optical density above 5 for all laser lines and a transmissivity in excess of 85% from 300–320 nm. An intensifier gate time of 50 ns and a low gain level of 60% minimised flame luminescence and noise. The detection system was calibrated using a multi-frequency target.

Aluminium oxide particles with $d_{p,90} < 1.66$ µm were used as velocity tracers. The Stokes number was below unity and the frequency response was sufficient for the smallest scales [20, 21]. Cross-correlation PIV with decreasing window size (256 × 256 to 32 × 32 with 50% overlap) was performed. The adaptive shape modulation of the interrogation windows incorporated the local flow field acceleration and provided a spatial resolution and vector spacing of $\lambda_{PIV} = 135.2$ µm [20]. The resolution $(3 \cdot L_\eta)$ and laser sheet thickness suggest that most (in-plane) fine scale flow structures were resolved. Out-of-plane contributions were insignificant [21].

3. Data Analysis

Bimodal two-fluid descriptions of turbulent reacting flows become inadequate at low Da [3]. Multi-fluid descriptions [20, 35] provide a more comprehensive delineation of chemically reacting flows where intermediate

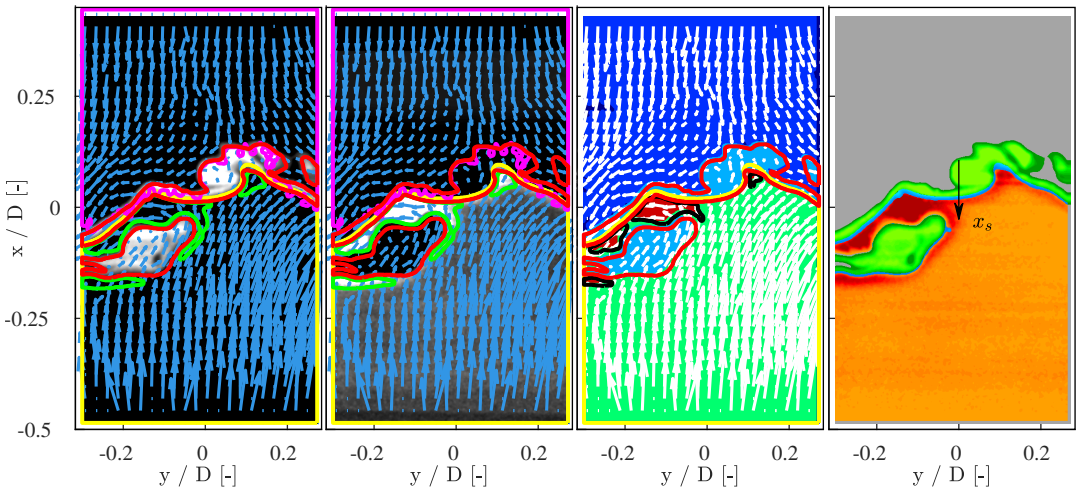

Figure 1: Sample images for DME / air, $\Phi = 0.50$, $T_{HCP} = 1600$ K. CH_2O–PLIF (left), OH–PLIF (2^{nd}) and multi-fluid (3^{rd}) image with iso-contours and PIV vectors overlaid (every sixth vector shown). The pink iso-contour encloses the reactants, yellow all OH signal, red the low temperature reacting fluid (i.e. CH_2O) and green the high temperature reacting fluid. Right image: Superimposed OH (orange – red), CH_2O (green), heat release layer (blue) and reactants (grey). The black arrow indicates the x_s coordinate system.

fluid states are statistically relevant. In previous work [13, 20, 21, 31], self-sustained flames were segregated from thermally supported burning by means of the thermochemical state at extinction. The bulk ($a_b \simeq 750$ s^{-1}) and mean turbulent strains ($a_I \simeq 3200$ s^{-1}) were significantly higher than the extinction strain ($a_q \simeq 190$ s^{-1}) of the corresponding laminar flames and self-sustained flames detached from the stagnation plane were not observed. A purpose written algorithm detected four iso-contours in each instantaneous image set (2000 images per condition) to distinguish between the different fluid states. Sample images (CH_2O, OH – PLIF and multi-fluid field) are shown in Fig. 1.

Reactant (R) Fluid: Fresh reactants emerging from the upper nozzle that have not undergone any thermal alteration were identified via a PIV particle seeding density segregation technique [20, 36].

Low Temperature Reactive (LTR) Fluid: Regions with a distinct CH_2O – PLIF signal in the absence of detectable OH levels [23].

Heat Release (HR) Fluid: Cross-correlation of CH_2O and OH – PLIF signals mark exothermic zones [2, 26].

High Temperature Reactive (HTR) Fluid: Regions with an OH – PLIF signal ≥ 2 times the HCP OH intensity were used to delineate high temperature DME oxidation [20].

Hot Combustion Products: The OH – PLIF signal close to the lower nozzle exit ($I^{\ddagger}$) was used to identify the HCP [20]. The detected iso-contour is related to the gas mixing layer interface [14].

3.1. Image Superposition and Spatial Resolution

Images of the multi-frequency calibration target from each camera system were used to create a common coordinate system and eliminate any residual spatial misalignment. This allows an accurate image superposition and is critical for the detection of the heat release layer ($CH_2O \times OH$). The spatial resolution of the detection system was measured using a NBS 1963A target and was $\sim 2 \cdot L_\eta$. Smoothing filter operations on the individual images resulted in a spatial multi-fluid resolution of $\lambda_{MF} = 250$ µm. The image dimensions were -14.6 < x < 12.9 and -9.0 < y < 8.2 mm resolved by 798 × 501 pixels. In comparison, the laminar flame thickness was 812 µm, the mean scalar dissipation layer thickness [37] $\lambda_D = 461$ µm and the Batchelor scale [38] $\lambda_B \simeq 82.3$ µm.

4. Results and Discussion

The investigated conditions occupy a nominally identical point in a classical combustion regime diagram (e.g. Borghi [39]) with $Re_t \simeq 350$, $Da \simeq 0.29$ and $Ka \simeq 64$. The burning mode changes were induced by variations in the thermal support with $1200 < T_{HCP}$ (K) < 1600. The data in Secs. 4.1 and 4.2 was conditioned on the theoretical stagnation point streamline (SPS) and aligned on the reaction onset iso-contour $x_s = 0$, see Fig. 1. The latter was detected by means of the density segregation technique or the first occurrence of either CH_2O or OH – LIF signals.

4.1. Multi–Fluid Flow Analysis

The reactant fluid probability drops (by definition) from unity to nil at the reaction onset $x_s = 0$ [20]. The low temperature reactive (LTR) fluid is depicted in the top of Fig. 2. The UN is at $x_s < 0$ and vice versa. The peak probability of the presence of formaldehyde directly adjacent to the reactants is 92% for $T_{HCP} = 1600$ K and reduces gradually to 48% for $T_{HCP} = 1200$ K. The probability is gradually reduced away from the origin with increasing T_{HCP} as more reactive fluid states are favoured. The spatial extent of the low temperature reactive fluid at high T_{HCP} is effectively limited by the integral length scale of turbulence (L_I) as formaldehyde is consumed by high temperature reactions (e.g. $CH_2O \times OH$). By contrast, the tail of the LTR probability extends to $2{\cdot}L_I$ for low T_{HCP}. This can be attributed to turbulent transport away from the reaction onset as the thermochemical state favours a persistent CH_2O concentration.

The probability of the heat release fluid (i.e. $CH_2O \times OH$ cross-correlation)

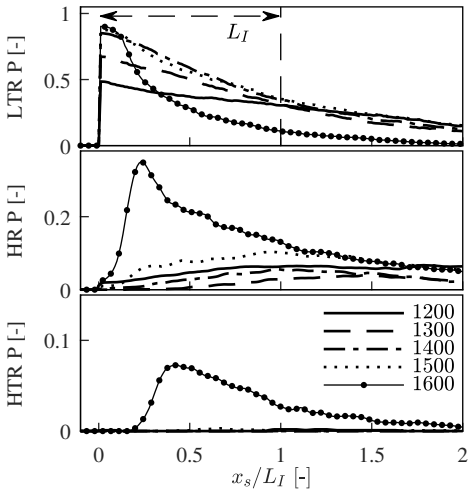

Figure 2: Multi-fluid probability statistics along the SPS and aligned at $x_s = 0$. Low temperature reactive (top), heat release (middle) and high temperature reactive fluid (bottom). Legend: T_{HCP} in [K].

is depicted in the middle of Fig. 2. Peak probabilities of 11 and 34% were determined for $T_{HCP} = 1500$ and 1600 K, respectively, with a peak value around 5% for lower T_{HCP}. The latter suggests that high temperature chain branching reactions are not triggered effectively. The peak location at $T_{HCP} = 1600$ K was $x_s/L_I \simeq 0.25$ and shifted away from the reaction onset to $x_s/L_I \simeq 1.0$ at $T_{HCP} = 1500$ K. The second can be attributed to turbulent mixing of the LTR fluid with the OH containing HCP resulting in a spatially distributed heat release zone. By contrast, the former case exhibits relatively thin formaldehyde layers that are quickly consumed by OH in exothermic reactions. The high temperature reactive fluid is only evident for $T_{HCP} = 1600$ K with a peak probability of $\sim$7.3% at $x_s/L_I \simeq 0.5$. The spatial extent was limited to 1.5 L_I, which can be attributed to dilatation. By contrast, Hampp and Lindstedt [20, 21] showed the presence of high temperature reactive fluids (i.e. distinct [OH] levels) in an ultra-lean ($\Phi = 0.20$) DME/air flame

supported at $T_{HCP} = 1700$ K. The comparison illustrates the importance of the external enthalpy source to the burning mode and reaction progress at low Da.

4.2. Scalar Profiles and Gradients

Mean normalised CH_2O and OH – PLIF ($I/I^{\ddagger}$) intensity profiles aligned at $x_s = 0$ are shown in the left column of Fig. 3. The OH contained in the HCP stream provides a constant and well-defined reference state (see Sec. 2.2) and the corresponding signal intensity close to the LN exit ($I^{\ddagger}$) was used for the normalisation. However, the current setup does not feature a similar reference state for the CH_2O concentration. Thus $I^{\ddagger}$ for the CH_2O signal was set to 1 count for a non-dimensional analysis. The statistics were compiled from at least 980 profiles and more than 1550 for $T_{HCP} \geq 1400$ K. The shape of the CH_2O distribution is relatively consistent with the peak located at $\sim L_I$. However, the peak intensity increases sixfold with increasing T_{HCP}. This compares well with the sevenfold increase of the CH_2O concentration obtained from corresponding laminar flames at a low rate of strain ($a = 75$ s^{-1}), see Table 2. The mean normalised OH intensities are close to unity for $x_s > 0$ at $T_{HCP} \leq 1400$ K. The absolute OH concentrations increase with temperature, see Table 1. High temperature chain branching is increasingly favoured for $T_{HCP} \geq 1500$ K and a distinct OH peak evolves. The latter is particularly prominent at $T_{HCP} = 1600$ K with a spatial extent similar to the HTR fluid peak in Fig. 2.

The maximum CH_2O and OH gradients (∇I_k) from the reactants to prod-

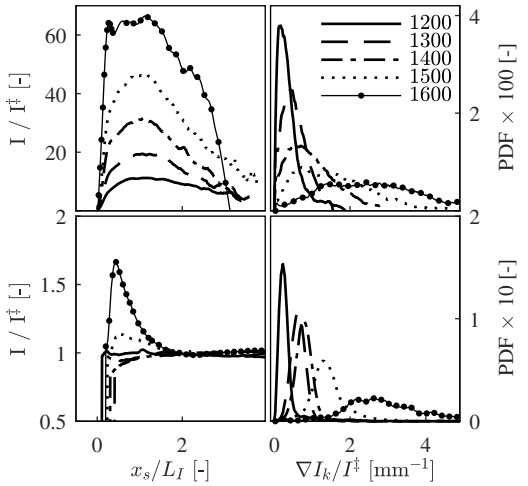

Figure 3: Mean CH_2O (top left) and OH – PLIF (bottom left) signal along with the PDF of the maximum normalised CH_2O (top right) and OH signal gradient (bottom right). The CH_2O gradients were scaled by 1/50 for visualisation on a shared axis. Legend: T_{HCP} in [K].

ucts were calculated using Eq. (2), where δ_x is the pixel spacing.

$$\nabla I_k = max\left(\frac{I_{k,i+1} - I_{k,i-1}}{I^‡ \cdot 2\delta_x}\right) \;;\quad \mathrm{k} = \mathrm{CH_2O,\ OH} \tag{2}$$

247 The mean resolution of the instantaneous 5–95% CH_2O peak at T_{HCP}

Table 2: Gradient of the normalised CH_2O and OH signal along with the 5 – 95% CH_2O layer thickness for $1200 < T_{HCP}$ (K) < 1600. The first and second three lines are the mean and mode of the PDFs in Figs. 3 – 4. The laminar δ_{CH2O} and normalised peak concentration ($\Lambda = [CH_2O]_{BTB}$ / $[CH_2O]_{twin}$) at $a = 75$ s^{-1} are also shown.

	$T_{HCP} \times 10^3$	[K]	1.20	1.30	1.40	1.50	1.60
Mean	∇I_{CH2O}	mm^{-1}	24	34	58	91	144
	∇I_{OH}	mm^{-1}	0.31	0.65	0.79	1.4	3.0
	δ_{CH2O}	mm	4.5	3.7	3.3	3.5	2.4
Mode	∇I_{CH2O}	mm^{-1}	8.3	18	28	33	131
	∇I_{OH}	mm^{-1}	0.21	0.61	0.81	1.3	2.7
	δ_{CH2O}	mm	3.1	2.4	1.5	1.4	1.3
Lam	Λ	–	0.86	0.85	0.71	0.36	0.11
	δ_{CH2O}	mm	2.2	1.8	1.1	0.91	0.87

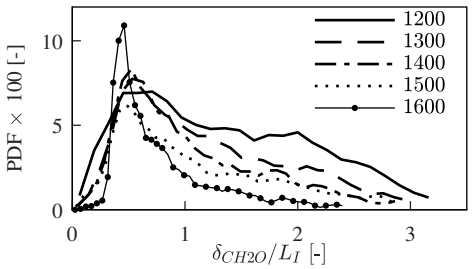

Figure 4: PDF of δ_{CH2O}. Legend: T_{HCP} in [K].

= 1600 K (narrowest peak) was resolved by 68±37 pixels. High frequency fluctuations of ∇I_k were removed using a low pass filter (length $\approx \lambda_{MF}$). The mean of the PDF(∇I_{CH_2O}) increases sixfold, see top right of Fig. 3, while the mode shifts from 8.3 to 131 mm^{-1} with increasing T_{HCP}. The mean of the PDF(∇I_{OH}) increases an order of magnitude with T_{HCP}, while the mode shifts from 0.21 to 2.7 mm^{-1} from 1200 $< T_{HCP}$ (K) <1600 K, see Table 2.

The PDF of the CH_2O layer thickness (δ_{CH2O}, 5 – 95% of the instantaneous maximum) illustrates a distinct broadening with decreasing T_{HCP} as depicted in Fig. 4. The mean of δ_{CH2O} decreases from 4.5 to 2.4 mm with increasing T_{HCP}. The mode of the PDF(δ_{CH2O}) at T_{HCP} = 1200 K is $\sim L_I$ and approaches δ_{CH2O} of the laminar flame calculations at higher T_{HCP}, see Table 2. The spatial distribution of the low temperature reactive zones with relatively narrow PDFs(∇I_k) for $T_{HCP} \leq 1300$ K can be attributed to turbulent mixing of HCP and reactants across the stagnation plane. The reaction progress is dominated by the thermochemical state of the burnt gases. By contrast, at higher T_{HCP} the flame assumes a flamelet–like structure with significantly increased intensity and gradients and reduced δ_{CH2O}.

4.3. Conditional Strain on Material Surfaces

The instantaneous planar rate of strain ($e_{ij} = 0.5(\partial u_i/\partial x_j + \partial u_j/\partial x_i)$) and vorticity ($\omega_{ij} = \partial u_i/\partial x_j - \partial u_j/\partial x_i$) tensors were calculated from the PIV data [21]. The normal ($a_n = f_{11}$) and tangential ($a_t = f_{22}$) strain components were determined by $f = \mathbf{R} \cdot e$, where $\mathbf{R}$ is the rotation matrix and Θ is the angle between the iso-contour normal and the SPS. The data was subsequently conditioned upon the multi-fluid iso-contours (β), where $\beta \equiv 1$ at the iso-contour and nil elsewhere. The total rate of strain was defined as $a_d = e_{11} + e_{22}$. The analysis includes the movement of the stagnation point in the radial limit $\pm$ 0.5 L_I away from the SPS [19].

The rate of strain along the reactant fluid iso-contour is only modestly affected by the T_{HCP} variation. The mean normal compressive ($a_n|R$), tangential ($a_t|R$) and total ($a_d|R$) strain and vorticity ($\omega|R$) were -1070 $\pm$ 158 s^{-1}, 419 $\pm$ 34 s^{-1}, -681 $\pm$ 100 s^{-1} and -668 $\pm$ 114 s^{-1}, respectively, with the PDF shapes maintained. The supplementary material contains a data summary.

4.3.1. Strain at the Low Temperature Reacting Surface

The conditional strain and vorticity along the low temperature reacting fluid material surface is depicted in Fig. 5. The means of PDF($a_n|LTR$) and PDF($a_t|LTR$) increase more than twofold from -568 $< a_n|LTR$ (s^{-1}) $<$ -1451 and 205 $< a_t|LTR$ (s^{-1}) $<$ 484 for 1200 $< T_{HCP}$ (K) $<$ 1600. The skewness of the PDFs($a_n|LTR$) towards reduced compressive strain increases with decreasing T_{HCP} with a mode shift from -1280 to -440. The spread was reduced by 22% from 1804 to 1410 s^{-1}. The PDFs($a_t|LTR$) are less skewed towards reduced extensive strains. The mean vorticity increases significantly with T_{HCP}. The elevated skewness towards reduced normal and tangential

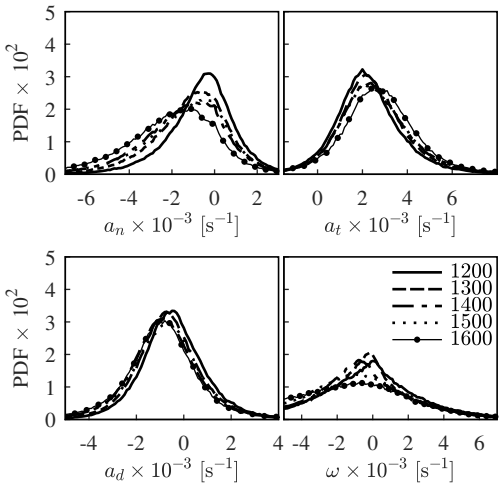

Figure 5: Rate of strain and vorticity evaluated along the low temperature reacting fluid surface: Normal (top left), tangential (right) and total (bottom left) strain and vorticity (right). Legend: T_{HCP} in [K].

strain with lower T_{HCP} can be attributed to the quenching of CH_2O in higher strain regions. At $T_{HCP} = 1600$ K formaldehyde is quickly consumed and appears in relatively thin layers.

4.3.2. Strain at the Heat Release Surface

The rate of strain on the heat release surface is depicted in Fig. 6. The mean PDF$(a_n|HR)$ increases twofold from -975 $< a_n|HR$ (s^{-1}) $<$ -1635 with increasing T_{HCP} and exhibits a mode shift from -900 to -1560 s^{-1}. The rms increases by $\sim$ 20% with T_{HCP}. The mean tangential strain increases at a similar rate to the PDFs$(a_t|LTR)$, while absolute values are on average $\sim$20% higher. The latter can be attributed to the enhanced dilatation. For $T_{HCP} \leq 1400$ K the heat release fluid was found in low strain pockets within the mixing layer of the stagnation plane. The vorticity levels were $> 30\%$ below corresponding reactant values. By contrast, at $T_{HCP} \geq 1500$ K the

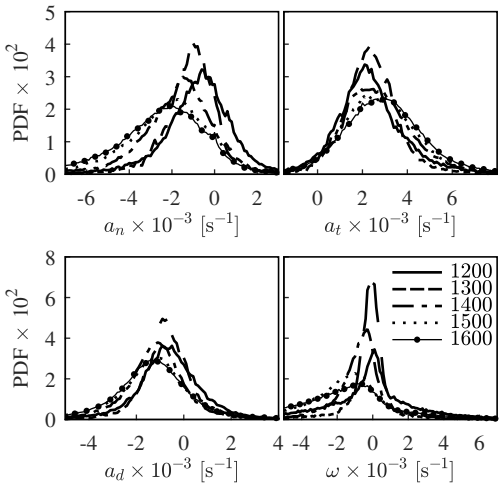

Figure 6: Rate of strain and vorticity evaluated along the heat release material surface: Normal (top left), tangential (right) and total (bottom left) strain and vorticity (right). Legend: T_{HCP} in [K].

heat release may occur in flamelet–like layers that survived elevated rates of strain. The high temperature reactive fluid was statistically relevant only for $T_{HCP} = 1600$ K. The mean normal compressive and tangential strains were -1975±2150 s^{-1} and 593±1390 s^{-1}, respectively.

5. Conclusions

The present work utilises a back-to-burnt opposed jet configuration for the aerodynamic stabilisation of lean ($\Phi = 0.50$) premixed DME/air flames with $Re_t \simeq 350$ and $Da = 0.29$ against hot combustion products. The HCP temperature was varied from 1200 to 1600 K. The results show that increasing thermal support temperatures close to or higher than the adiabatic flame temperature (1536 K) gradually favours flamelet–like structures. The latter were characterised by steep scalar gradients, thin CH_2O layers and a sequential occurrence of preheat, heat release and high temperature flame

zones. Such reaction zones survived relatively high rates of strain. However, the overall likelihood remained comparatively low (i.e. $\sim$30%). By contrast, lower T_{HCP} lead to a spatial distribution of low temperature reactive zones with significantly reduced species gradients and peak levels. Significant high temperature chain branching (i.e. distinct OH levels) was not observed for $T_{HCP} \leq 1400$ K. The spatially distributed heat release ($CH_2O \times OH$) of the thermally supported burning occurred within the HCP. In comparison to the low temperature reactive fluid, the underlying normal strain increased due to the proximity to the stagnation plane, while the increase in extensive tangential strain was attributed to dilatation. The burning mode and the reaction progress of low Da reacting flows is strongly dependent on the thermochemical state of the external enthalpy source. The current data set provides an excellent challenge for existing turbulent combustion models and supports the development of new models that are applicable in regimes that are not covered by conventional combustion regime diagrams.

Acknowledgements

The authors would like to acknowledge the support of the AFOSR and EOARD under Grant FA9550-17-1-0021 and the encouragement by Dr. Chiping Li and Dr. Russ Cummings. The US Government is authorised to reproduce and distribute reprints for Governmental purpose notwithstanding any copyright notation thereon. Mr Hamed Shariatmadar wishes to gratefully acknowledge the receipt of an Imperial College President's PhD Scholarship Award for outstanding students. The authors would also like to thank Dr. Robert Barlow.

References

[1] V. D. Milosavljevic, R. P. Lindstedt, M. D. Cornwell, E. J. Gutmark, E. M. Váos, in G. Roy, K. H. Yu, J. H. Whitelaw, J. J. Witton (Eds.), Advances in Combustion and Noise Control, Cranfield University Press, 2006, pp. 149–165.

[2] Y. Minamoto, N. Swaminathan, Combust. Flame 161 (2014) 1063–1075.

[3] Y. Minamoto, N. Swaminathan, R. S. Cant, T. Leung, Combust. Sci. Technol. 186 (2014) 1075–1096.

[4] F. J. Weinberg, Nature 233 (1971) 239–241.

[5] E. Mastorakos, A. Taylor, J. Whitelaw, Combust. Flame 102 (1995) 101–114.

[6] R. Lückerath, W. Meier, M. Aigner, J. Eng. Gas Turb. Power 130 (2008) 011505.

[7] J. A. Wünning, J. G. Wünning, Prog. Energ. Combust. 23 (1997) 81–94.

[8] P. Sabia, M. de Joannon, A. Picarelli, R. Raguccia, Combust. Flame 160 (2013) 47–55.

[9] B. Zhou, C. Brackmann, Q. Li, Z. Wang, P. Petersson, Z. Li, M. Aldén, X.-S. Bai, Combust. Flame 162 (2015) 2937–2953.

[10] B. Zhou, C. Brackmann, Z. Li, M. Aldén, X.-S. Bai, Proc. Combust. Inst. 35 (2015) 1409–1416.

[11] B. Zhou, Q. Li, Y. He, P. Petersson, Z. Li, M. Aldén, X.-S. Bai, Combust. Flame 162 (2015) 2954–2958.

[12] B. Zhou, C. Brackmann, Z. Wang, Z. Li, M. Richter, M. Aldén, X.-S. Bai, Combust. Flame 175 (2016) 220–236.

[13] F. Hampp, PhD thesis, Imperial College, May 2016, url: http://hdl.handle.net/10044/1/32582.

[14] B. Coriton, J. H. Frank, A. Gomez, Combust. Flame 160 (2013) 2442–2456.

[15] K. H. H. Goh, P. Geipel, F. Hampp, R. P. Lindstedt, Proc. Combust. Inst. 34 (2013) 3311–3318.

[16] B. Böhm, C. Heeger, I. Boxx, W. Meier, A. Dreizler, Proc. Combust. Inst. 32 (2009) 1647–1654.

[17] K. H. H. Goh, P. Geipel, F. Hampp, R. P. Lindstedt, Fluid Dyn. Res. 45 (2013) 061403.

[18] D. Geyer, A. Kempf, A. Dreizler, J. Janicka, Combust. Flame 143 (2005) 524–548.

[19] P. Geipel, K. H. H. Goh, R. P. Lindstedt, Flow Turbul. Combust. 85 (2010) 397–419.

[20] F. Hampp, R. P. Lindstedt, Combust. Flame 182 (2017) 248–268.

[21] F. Hampp, R. P. Lindstedt, Proc. Combust. Inst. 36 (2017) 1911-1918.

[22] F. Hampp, R. P. Lindstedt, in A. Runchal, A. Gupta, A. Kushari, A. De (eds.) Energy for Propulsion, Springer-Verlag, To Appear.

[23] R. L. Gordon, A. R. Masri, E. Mastorakos, Combust. Flame 155 (2008) 181–195.

[24] S. H. Won, B. Windom, B. Jiang. Y. Ju, Combust. Flame 161 (2014) 475–483.

[25] B. O. Ayoola, R. Balachandran, J. H. Frank, E. Mastorakos, C. F. Kaminski, Combust. Flame 144 (2006) 1–16.

[26] R. L. Gordon, A. R. Masri, E. Mastorakos, Combust. Theor. Model. 13 (2009) 645–670.

[27] J. R. Osborne, S. A. Ramji, C. D. Carter, S. Peltie, S. Hammack, T. Lee, A. M. Steinberg, Exp Fluids 57 (2016) 65.

[28] J. R. Osborne, S. A. Ramji, C. D. Carter, A. M. Steinberg, Proc. Combust. Inst. 36 (2017) 1835–1841.

[29] K. H. H. Goh, P. Geipel, R. P. Lindstedt, Combust. Flame 161 (2014) 2419–2434.

[30] K. H. H. Goh, P. Geipel, R. P. Lindstedt, Proc. Combust. Inst. 35 (2015) 1469–1476.

[31] F. Hampp, R. P. Lindstedt, In Y. Sakai and C. Vassilicos (eds.) Fractal Flow Design: How to Design Bespoke Turbulence and why, Springer-Verlag, CISM Int. Mech. Sci. 568, 2016, 75–102.

[32] N. Peters, in: W. A. Sirignano, A. G. Merzhanov, L. De Luca (eds.), Advances in Combustion Science: In Honor of Y. B. Zel'dovich, AIAA, Prog. Astronaut. Aeron. 173 (1997) 73–91.

[33] S.-W. Park, PhD thesis, Imperial College, March 2012, url: http://hdl.handle.net/10044/1/9599.

[34] S. A. Skeen, J. Manin, L. M. Pickett, Proc. Combust. Inst. 35 (2015) 3167–3174.

[35] D.B. Spalding, Proc. 7^{th} Biennial Conf. on Comp. Techn. Appl. (CTAC 95), World Scientific Publishing Co Ltd, (1996) 59–81.

[36] A. M. Steinberg, J. F. Driscoll, S. L. Ceccio, Exp. Fluids 44 (2008) 985–999.

[37] K. A. Buch, W. J. A. Dahm, J. Fluid Mech. 364 (1998) 1–29.

[38] G. K. Batchelor, J. Fluid Mech. 5 (1959) 113–133.

[39] N. Peters, J. Fluid Mech. 384 (1999) 107–132.

List of Tables

List of Figures

List of Supplementary Material

Figure S1 Schematic of the experimental configuration. SP – stagnation plane; DSI – density segregation iso-contour; HCP – hot combustion products; CFG – cross fractal grid; PP – Perforated plate; x,y – Coordinate system.

Table S1 Summary of the normal (a_n), tangential (a_t) and total (a_d) strain and vorticity (ω) conditioned upon the material surfaces (β) for DME/air mixtures at $\Phi = 0.5$, $Re_t = 350$ and $Da = 0.29$ for a HCP temperature variation in the range $1200 < T_{HCP}$ (K) < 1600. Listed are the mode, mean and spread of the respective PDFs. R – reactants; LTR – low temperature reactive; HR – heat release (i.e. CH_2O – OH cross-correlation); HTR – high temperature reactive; HCP – hot combustion product fluid iso-contour.